Large eddy simulation of boundary-layer turbulence over the heterogeneous surface in the Source Region of the Yellow River

Yunshuai ZHANG[1], Qian HUANG[1,*], Yaoming MA[1,2,3,4], Jiali LUO[1], Chan WANG[5], Zhaoguo LI[5], and Yan CHOU[1]

[1] *Key Laboratory for Semi-Arid Climate Change of the Ministry of Education, College of Atmospheric Sciences, Lanzhou University, Lanzhou* 730000, *China*

[2] *Land-Atmosphere Interaction and its Climatic Effects Group, State Key Laboratory of Tibetan Plateau Earth System, Resources and Environment (TPESRE), Institute of Tibetan Plateau Research, Chinese Academy of Sciences, Beijing 100101, China*

[3] *University of Chinese Academy of Sciences, Beijing* 100049, *China*

[4] *CAS Center for Excellence in Tibetan Plateau Earth Sciences, Chinese Academy of Sciences, Beijing* 100101, *China*

[5] *Key Laboratory of Land Surface Process and Climate Change in Cold and Arid Regions, Northwest Institute of Eco-Environment and Resources, Chinese Academy of Sciences, Lanzhou* 730000, *China*

Abstract

Lake breezes are proved by downdrafts and the divergence flows of zonal wind in the source region of the Yellow River (SRYR) in the daytime based on ERA-Interim reanalysis data. In order to depict the effect of the circulations induced by surface anomaly heating (patches) on the boundary-layer turbulence, the large eddy model was used to produce a set of 1D strip-like surface heat flux distributions based on observations, which obtained by a field campaign in the Ngoring Lake Basin in the summer of 2012. The simulations show that for the cases without background wind, patch-induced circulations (SCs) promote the growth of convective boundary layer (CBL), enhance the turbulent kinetic energy (TKE) and then modify the spatial

*Corresponding author.
E-mail address: huangq@lzu.edu.cn (Q. Huang).

删除[zhangysh]: [a]

删除[zhangysh]: [a]

删除[zhangysh]: [a]

删除[zhangysh]: [b]

删除[zhangysh]: [c]

删除[zhangysh]: [d]

删除[zhangysh]: [a]

删除[zhangysh]: [e]

删除[zhangysh]: [e]

删除[zhangysh]: [a]

删除[zhangysh]: [a]

删除[zhangysh]: [b]

删除[zhangysh]: *Key Laboratory of Tibetan Environment Changes and Land Surface Processes, Institute of Tibetan Plateau Research, Chinese Academy of Sciences, Beijing* 100101, *China*

删除[zhangysh]: [c]

删除[zhangysh]: [d]

删除[zhangysh]: [e]

删除[zhangysh]: ambient

删除[zhangysh]: s

distribution of TKE. Based on phase-averaged analysis, which separates the attribution from the SCs and the background turbulence, the SCs contribute no more than 10% to the vertical turbulent intensity, but their contributions to the heat flux can be up to 80%. The thermal internal boundary layer (TIBL) reduce the wind speed and form the stable stratification, produce the obvious change of turbulent momentum flux and heat flux over the heterogeneous surfaces. The increased downdrafts, which mainly occur over the lake patches and carry more warm, dry air down from the free atmosphere. The background wind inhibits the SCs and the development of the CBL, it also weakens the patch-induced turbulent intensity, heat flux, and convective intensity.

Key word: turbulence, heat flux, heterogeneously surface heating, background wind, phase-averaged analysis

1. Introduction

Turbulence in the planetary boundary layer (PBL), which is derived from surface heating and surface fraction, plays an important role in the exchange of heat, momentum, moisture, and chemical constituents between the surface and free atmosphere (Zhang et al., 2018). Previous studies on the turbulence and turbulent exchange over homogeneous surfaces based on Monin-Obukhov similarity theory were conducted before the 1990s (Sommeria and LeMone, 1978; Moeng, 1984). Then turbulence over heterogeneous surfaces was investigated through field campaigns (Wang et al., 2016; Zhao et al., 2018) and numerical simulations (Shao et al., 2013; Liu et al., 2011) in the past few decades, which help us better understand the

设置格式[zhangysh]: 非突出显示

设置格式[zhangysh]: 非突出显示

删除[zhangysh]: The lake patches produce consistent spatial distributions of wind speed and turbulent stress over the lake–land boundary, and the obvious change of turbulent momentum flux over the boundary of patches can not be neglected. In the entrainment layer, the convective rolls still persist under stronger geostrophic winds of 7–11 m s^{-1}.

删除[zhangysh]: In general, the SCs promote the growth of convective boundary layer, while the background flows inhibit it.

删除[zhangysh]: s

删除[zhangysh]: flows

删除[zhangysh]:

设置格式[zhangysh]: 两端对齐，缩进: 左侧: 0 毫米，左 0 字符，首行缩进: 5 字符

删除[zhangysh]: Turbulence

interactions between the surface and atmosphere. Thermal surface heterogeneity is a typical issue and leads to the formation of local/secondary circulations. Sea and lake breezes are a well-known example of flows that are generated by heterogeneous surface heating between the land and water (Crosman and Horel, 2012). Observations have also revealed the imbalance in the surface energy budget over heterogeneous surfaces (Foken et al. 2010; Xu et al., 2016). The most widely used eddy covariance (EC) system for a single site has been shown to underestimate the turbulent flux due to the large-eddy transport or secondary circulations not being captured (Foken et al., 2010; Xu et al., 2016). The simulation studies conducted by Zhou et al. (2018) and Frederik and Matthias (2018) showed that the flux induced by mesoscale or secondary circulations is the main reason for the energy imbalance. Moreover, the PBL parameterization schemes in the weather/climate model over a heterogeneous surface have been continuously improved until now (Avissar and Pielke, 1989; Shao et al., 2013). Different surface patterns such as mosaic (Avissar and Schmidt, 1998), chessboard (Liu et al., 2011; Shen et al., 2016), patchy-like (Zhou et al., 2018), and strip-like (Li et al., 2011; Wang et al., 2011) patterns have been utilized to simulate thermodynamic surface heterogeneity. These studies confirmed that the secondary circulation induced by the surface heterogeneity influences the PBL's properties and turbulent characteristics. In addition, several studies have examined the effects of surface heterogeneity on different levels of background wind (Shen and Leclerc, 1995; Liu et al., 2020) and the direction relative to the orientation of the heterogeneity (Wang et al., 2011; Kang and Lenschow, 2014), as well as the spatial and temporal

删除[zhangysh]: which has improved our understanding of the transfer and spatial and temporal variability of the turbulence.

删除[zhangysh]: s

variations of the wind fields (Liu et al., 2018). However, the issues related to the effects of the surface heterogeneity in special areas still need to be explored.

The dynamic and thermodynamic influences of the Tibetan Plateau (TP) on the regional and global weather and climate systems are closely related to its PBL, and turbulence plays a significant role in the mass and energy exchange between the TP and the atmosphere (Chen et al., 2013; Chen et al., 2016). Different landscapes make up the heterogeneous land surface over the TP. As the Asian Water Tower, lakes are widely and densely distributed over the TP, which affects the overlying energy and mass transport through the lake-air turbulent heat flux. Biermann et al. (2014) and Wang et al. (2015) discovered that the turbulent flux of Lake Nam co, which is surrounded by wet grasslands, is actually very considerable but was often underestimated by a hydrodynamic multilayer model from Foken (1979 and 1984). 删除[zhangysh]: in the model

The Source Region of the Yellow River (SRYR) is located in the northeastern part of the TP and is known as the “water tower” of China because it contains 48 lakes. The Ngoring and Gyaring (Sisters) Lakes are two major lakes, and Ngoring Lake is the largest in the SRYR (Li et al., 2015; Wen et al., 2015). In addition to the lakes, the forests, alpine meadow, wetlands, rivers, and glaciers comprise the diverse underlying surfaces in the SRYR, with grassland accounting for about 80% of the area (Mudassar et al., 2018). Consequently, the SRYR is an ideal region for studying the turbulence over a heterogeneous land surface.

Observational studies have revealed that water vapor, heat and energy exchange 删除[zhangysh]: ,
occur over alpine meadows/wetlands (Zheng et al., 2015; Jia et al., 2017) and lakes

(Li et al., 2015; Wen et al., 2016), and models have been used to simulated the effects of the lakes on the cool and moist regional climate (Wen et al., 2015; Ao et al., 2018). However, the features of the boundary-layer turbulence over the heterogeneous underlying surfaces and the effects of thermodynamic surface heterogeneity on the turbulent flux in the SRYR remain unclear. Over the last few decades, the lakes have shrunk and the grasslands have degraded in the SRYR due to climate change and the excessive utilization of water resources (Brierley et al., 2016; Mudassar et al., 2018). It is essential to investigate the variation in the structure of boundary-layer and turbulent heat flux with changes in the surface's thermal properties and the background wind.

删除[zhangysh]: s

High resolution field measurements are extremely rare on the TP because of the harsh environmental conditions, so few observational studies on the turbulence characteristics and the turbulent heat flux have been conducted. Large eddy simulation (LES) has the unique advantage of being accurate and able to describe turbulence finely, and thus, it has been widely used to investigate the effects of surface heterogeneity on turbulence (Hadfield et al., 1991, 1992; Kang and Lenschow, 2014). However, little has been done to improve our understanding of how the surface heterogeneity affects the boundary-layer turbulence, and the contributions of the patch-induced motions to the turbulent flux and energy in the SRYR. Furthermore, modeling the turbulence over the heterogeneous surface in the SRYR can not only lay a basis for the analysis of the local energy and mass transport, but it can also provide a quantitative reference for improving the parameterization schemes over

heterogeneous surfaces in weather and climate models.

In this study, we used LES to investigate the detailed turbulence characteristics in the SRYR. Our primary focus was the impacts of the surface heat flux anomalies on the turbulent kinetic energy (TKE), turbulent intensity, and turbulent flux. The turbulence characteristics and turbulent fluxes in the surface and the entrainment layers of PBL were investigated, too. This paper is arranged as follows Section 2 describes the model and data used in this study. Section 3 discusses the modeled results in detail, and section 4 provides a summary and discussion of our findings.

2 Data and methods

删除[zhangysh]: **d**

2.1 Study area and observations

Ngoring Lake and Gyaring Lake (hereinafter referred to as the two lakes) are located in the SRYR and are surrounded by the alpine meadow. Their mean elevation is 4274 m above sea level. The study area is shown in Fig. 1. The turbulent flux and standard atmospheric variables were measured over the lake and grassland surface. The GPS radiosonde data from the field campaign on July 29, 2012, at 30 m west of Lake Ngoring (near the gradient tower station, TS) and Madoi station (MD) located 30 km the east of the lake (34.918° N, 98.216° E, 4279 m AMSL). The eddy covariance data for Lake Station (LS) above the northwest of the lake (35.026° N, 97.652° E) and Grassland Station (GS) (34.913° N, 97.553° E) at 1.5 km west of the lake shore were used. For further details on the field campaign and the quality control of the sounding and eddy covariance data, see Li et al. (2015) and Li et al. (2017). The synoptic background at 500 hPa and the distribution of the wind components in

删除[zhangysh]: f

删除[zhangysh]: at

删除[zhangysh]: , as well as t

删除[zhangysh]: near the surface and

the vertical and horizontal directions were investigated using the ERA-Interim Reanalysis Data with a 0.25° × 0.25° resolution collected at 12:30 LT and 18:30 LT (LT: local time, used in the whole study) on July 29, 2012, with a delimiting a range of 32° N–37° N, 95° E–100° E, including the two lakes area (34.8° N–35° N, 97° E–98° E) and the surrounding grassland.

删除[zhangysh]: 1°×1°

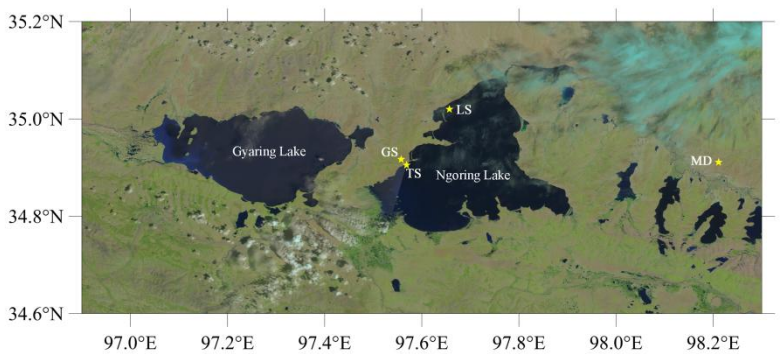

Figure 1. Map of the study area obtained using Landsat data on 21th August, 2014, with the location of the observation stations marked by yellow stars. The turbulent fluxes were measured at LS and GS stations. The standard atmospheric variables were observed at the TS. MD is a fixed meteorological observatory of the China Meteorological Administration.

删除[zhangysh]: .

2.2 Methods

2.2.1 Simulations set-up over the heterogeneous underlying surface

The U.K. Met Office large eddy model (LEM) version 2.4 (Gray et al., 2001) was used in this paper. The LEM is a three-dimensional and non-hydrostatic numerical model, which can be used to simulate a wide range of turbulence-scale and cloud-scale problems with a high resolution. The domain size was 135 km × 30 km × 6 km in the *y*, *x* and *z* direction respectively, with a horizontal grid-spacing of 200 m. According to Honnert et al. (2011) and Honnert et al. (2020), the horizontal resolution of 200 m is reasonable in this LEM study. There were 74 levels in the vertical direction, with a vertically stretched grid having a minimum spacing of 1.1 m in the

surface layer and a maximum of 64.8 m above 2000 m. Periodic lateral boundary conditions were applied, with a rigid lid at the top of the model domain. To reduce the reflection of the internal gravity waves, a Newtonian damping layer was applied above 3500 m. The surface boundary conditions of the model were derived from the Monin-Obukhov similarity theory using the Businger-Dyer functions. The subgrid model used in the LEM was based on the Smagorinsky-Lilly approach (Brown et al., 1994). The potential temperature, wind (u and v), and relative humidity profiles obtained during the field campaign on July 29, 2012, were used to initialize the 3D runs. The LEM was driven by the time-varying sensible heat flux (SHF) and the latent heat flux (LHF) at the surface. The geostrophic wind shear was calculated using the ERA-Interim geostrophic wind at the surface and at 1500 m. These conditions will be detailed on Fig. 2. The simulation time was 12 hours and the data were output every hour. The time step is 0.01s for all simulations. In this study, twelve 3D runs with different surface heat flux under various background wind conditions were performed. Two of the runs were horizontally homogeneous with a uniform grass surface under the conditions of wind (HOMW) and no wind (HOM). The other cases were simulated with one (A1L) or two (A2L) lake patches in the middle of the model domain. The surface heat flux anomaly was applied over a 30 km wide strip (two strips for A2L) extending the entire 30 km width of the domain in the x-direction. Here the term heat flux refers to both the sensible and latent heat fluxes. This can be viewed as representing Ngoring Lake and Gyaring Lake in the SRYR. It should be noted that in this study the scale of the heterogeneity was large enough to enable the

删除[zhangysh]: A vertically stretched grid with a minimum spacing of 1.1 m was utilized in the surface layer and a maximum of 64.8 m above 2000 m.

删除[zhangysh]: es

删除[zhangysh]: ambient

formation of small eddies over the lake patches that could coexist with the large-scale patch-induced circulations (Patton et al., 2005). Four simulations (A1L, A2L, A1LW, and A2LW) were initialized using the surface heat flux over the patch/patches measured at LS and the heat flux outside the patch/patches measured at GS. This means that the heat flux into the modeled atmosphere decreases as the number of patches increases. However, it is helpful to separate the effects of the total increase in heating from the effects of the localization of the heating when considering the consequences of an unresolved spatially changing heat flux for a global model. In order to keep the total heat flux in the modeled atmosphere constant, a "balanced" surface heat flux approach was used. Therefore, if the surface heat flux observed at the GS is denoted as FGS, and the heat flux over the patch and outside of the patch

删除[zhangysh]: es

are denoted as FL and FG, respectively. FL and FG were calculated using the following equations:

$$FL = FGS \times (SL/ST) \quad (1)$$

$$FG = FGS \times (SG/ST) \quad (2)$$

where ST, SL, and SG are the squares of the model domain, the patch, and the outside of it, respectively. Another four simulations (A1LC, A2LC, A1LWC, and A2LWC) were performed using this balanced surface heat flux approach. The heterogeneous initial conditions were used in the surface heat flux anomaly simulations. The initial profiles over the patch/patches were derived using the data from TS station, and the data observed at the MD station used for the outside patch/patches. Various background wind conditions were also used for the surface heat flux anomaly runs.

删除[zhangysh]: A1L_C

删除[zhangysh]: A2L_C

删除[zhangysh]: A1LW_C

删除[zhangysh]: A2LW_C

删除[zhangysh]: ambient

The parameters and the conditions of each run are listed in Table 1 for convenience. Sketches of the heterogeneous surface and of the surface heat flux over the lake patches and the outside patches for the unbalanced and balanced cases are depicted in Fig. 2.

The initial potential temperature and special humidity are shown in Fig. 2h, and the horizontal components of the wind profiles and the geostrophic wind are shown in Fig. 2g. A stable layer was found over the grass and a 200 m convective boundary layer (CBL) was found over the lake at 06:30 LT. The special humidity profiles show that the air tends to be moister over the lake (dash lines in Fig. 2h). The study area is characterized by a considerable surface heat flux and high wind speeds in the daytime. The stronger initial velocity is from the GS, which recorded wind speeds of up to 10 $m \cdot s^{-1}$ below 500 m.

删除[zhangysh]: es

删除[zhangysh]: f

删除[zhangysh]: f

删除[zhangysh]: f

删除[zhangysh]: f

Table 1

Parameters for the 3D simulations over the homogeneous surface (HOM) and heterogeneous surface with surface heat flux anomalies (A) under different conditions: with one (1L) or two (2L) lake patches, with initial wind and geostrophic wind (W), without geostrophic wind (NG), with the constant surface heat flux (C).

Name	Wind field	Surface heat flux (SHF and LHF)	Number of lake patches	Size of Lake patch (km)
HOM	without wind	FGS	0	-
HOMW	initial wind + geostrophic wind	FGS	0	-

A1L	without wind	lake patch: FLS (Heat flux that observed at LS); outside patch: FGS	1	30
A2L	without wind	lake patches: FLS (Heat flux that observed at LS); outside patches: FGS	2	30 and 30
A1LW	initial wind + geostrophic wind	Same as A1L	1	30
A2LW	initial wind + geostrophic wind	Same as A2L	2	30 and 30
A1LNG	initial wind	Same as A1L	1	30
A2LNG	initial wind	Same as A2L	2	30 and 30
A1LC	without wind	lake patch: (SL/ST) ×FGS =(30/135)× FGS; outside patch: (SG/ST)×FGS =(105/135)×FGS	1	30
A2LC	without wind	lake patches: (SL/ST)×FGS =(30/135)×FGS; outside patches: (SG/ST)×FGS =(75/135)×FGS	2	30 and 30
A1LWC	initial wind + geostrophic wind	Same as A1LC	1	30
A2LWC	initial wind + geostrophic wind	Same as A2LC	2	30 and 30

删除[zhangysh]: A1L_C

删除[zhangysh]: A2L_C

删除[zhangysh]: A1LW_C

删除[zhangysh]: A1L_C

删除[zhangysh]: A2LW_C

删除[zhangysh]: A2L_C

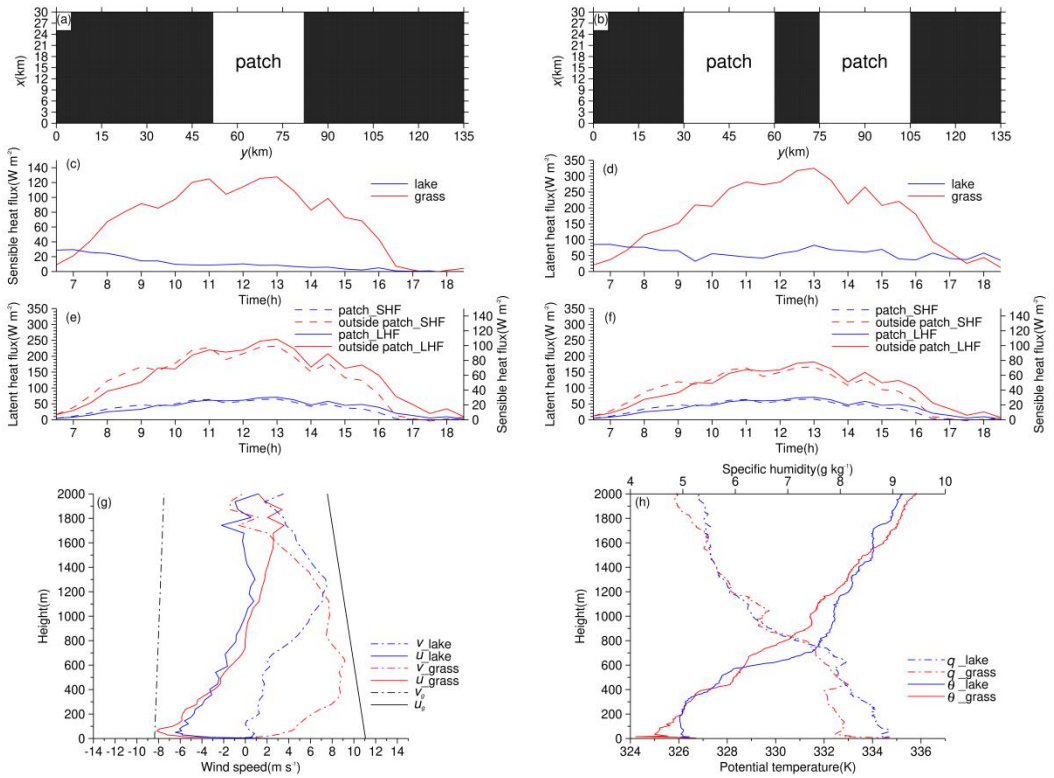

Figure 2. Sketch of the heterogeneous surface (a and b), surface sensible heat flux and latent heat flux (c and d) over the grassland (red line) and the lake (blue line) from observation. The SHF and the LHF for runs with (e) one and (f) two lake patches and a constant heat flux. Figs. 2g and 2h show the model initial profiles of the winds (solid lines for u, dash lines for v), potential temperature (solid lines), and special humidity (dash lines) over the lake patches (blue lines) and outside of the patches (red lines). The input geostrophic winds are also shown (black lines).

删除[zhangysh]: .

删除[zhanysh]: (c and d)

删除[zhangysh]: ure

2.2.2 statistical analysis

According to turbulence theory, a physical quantity ϕ has two parts, i.e., the horizontal average $\langle\phi\rangle$ and the turbulent fluctuation ϕ', so

删除[zhangysh]: and

$$\phi = \langle\phi\rangle + \phi' \tag{3}$$

This equation usually works in cases with a homogeneous surface. The variances of velocity and the potential temperature variances (σ_v^2, σ_w^2, σ_θ^2) are calculated from v', w', and θ', respectively. For a heterogeneous surface, phase-averaged analysis helps separate the patch-induced circulations from the random turbulent motions. This

method has been applied in studies of the one-dimension and two-dimension heterogeneities (Matthias et al., 2014; Kang and Lenschow, 2014; Shen et al., 2016), as well as the complex and irregular heterogeneities (Maronga and Raasch, 2013). In this study, one-dimensional heterogeneous (in the y direction) simulations were performed for which ϕ can be decomposed into three parts:

$$\phi = \langle \phi \rangle + \phi_{hi} + \phi_s \tag{4}$$

Where $\langle \phi \rangle$ is the horizontal average; ϕ_{hi} is the heterogeneity-induced part which is the averaged ϕ across the domain in the y direction; and ϕ_s is from the background turbulence. The variances of velocity and the potential temperature induced by the heterogeneity ($[\sigma_v^2]_{hi}$, $[\sigma_w^2]_{hi}$, $[\sigma_\theta^2]_{hi}$) are calculated from v_{hi} , w_{hi} , and θ_{hi} , respectively.

Phase-averaged analysis was also used to obtain the patch-induced component of the turbulent fluxes. We multiplied w and ϕ with both in the forms of Equation (4), and derived the total vertical transport of ϕ:

$$\overline{\langle w\phi \rangle} = \overline{\langle w \rangle \langle \phi \rangle} + \langle w_{hi} \phi_{hi} \rangle + \overline{\langle w_s \phi_s \rangle} \tag{5}$$

Since the horizontal average vertical velocity $\langle w \rangle$ is approximately zero in the LES, the turbulent fluxes were divided into two parts: circulations induced part and background turbulence induced part:

$$\overline{\langle w\phi \rangle} = \langle w_{hi} \phi_{hi} \rangle + \overline{\langle w_s \phi_s \rangle} \tag{6}$$

Moreover, the total kinetic energy e can be written as two parts, e_{hi} and e_s, which represent the contributions from the patch-induced and background turbulence:

$$e = e_{hi} + e_s \tag{7}$$

删除[zhangysh]: and

删除[zhangysh]: a patch-induced

删除[zhangysh]: a

$$e_{hi} = \left(\left\langle u_{hi}^{\,2}\right\rangle + \left\langle v_{hi}^{\,2}\right\rangle + \left\langle w_{hi}^{\,2}\right\rangle\right)/2 \quad (8)$$

$$e_s = \left(\left\langle u_s^{\,2}\right\rangle + \left\langle v_s^{\,2}\right\rangle + \left\langle w_s^{\,2}\right\rangle\right)/2 \quad (9)$$

3. Results

3.1. Synoptic background and wind components' distributions

In order to investigate the existence of a daytime (6:30-18:30 LT) lake breeze (the divergent flows over the lake surface and the downdrafts overlying it) using the ERA-Interim reanalysis data with a 0.25° × 0.25° resolution for the two lakes area (34.8° N–35° N, 97° E–98° E; blue box in Fig. 3), the wind field, temperature field, and geopotential height field at 500 hPa (~5500 m) at 12:30 LT and 18:30 LT on July 29, 2012 were analyzed. The southerly wind controlled the entire region at 500 hPa at 12:30 LT (Fig. 3a) then it became divergent flow at 18:30 LT (Fig. 3b). The vertical sections of the two wind components (u and w) were also depicted to further ascertain the distribution of the wind field in the longitude and latitude directions. It should be noted that downdrafts are dominant below 500 hPa in the two lakes area during the day (Figs. 3c and 3d). As can be seen from Fig. 3f, distinct divergent zonal wind (u) flows existed in the two lakes area at 18:30 LT. The wind speed derived from the GPS sounding at 12:30 LT is larger than that at 18:30 LT below 2 km (see Fig. S1 in supplement), indicating that the larger background wind covered up the divergent wind at 12:30 LT. Evidently, it is difficult to directly observe the lake breeze circulation due to the synoptic background, but the downdrafts and the divergent zonal wind in the two lakes area demonstrate the existence of a lake breeze. In the following sections, the turbulence characteristics over the heterogeneous underlying

删除[zhangysh]: f

删除[zhangysh]: at the surface (600 hPa, ~4200 m) and

删除[zhangysh]: ,

删除[zhangysh]: A cyclone controlled the entire region above the surface at 12:30 LT (Fig. 3a) and divergent flow occurred at 500 hPa at 18:30 LT (Fig. 3b)

删除[zhangysh]: f

删除[zhangysh]: f

删除[zhangysh]: flows

删除[zhangysh]: flow

surface are simulated and the effects of the patch-induced circulation are analyzed.

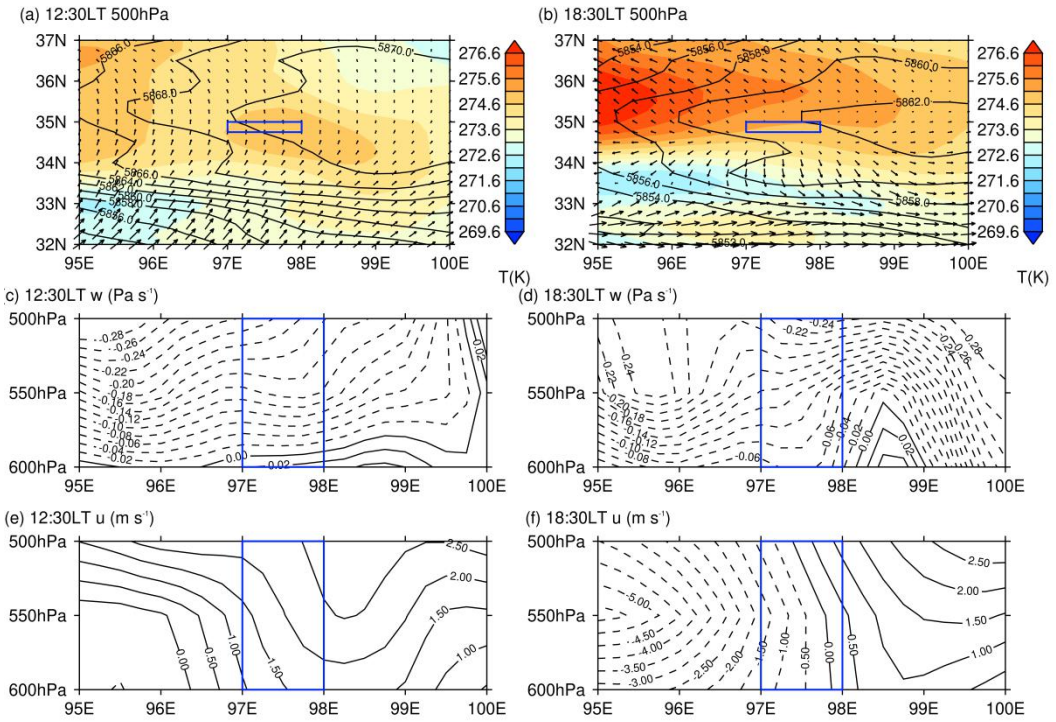

Figure 3. Synoptic background on July 29, 2012. Blue boxes represent the two lakes area. (a) and (b) show the wind field, temperature field, and geopotential height field at 500 hPa (~5500 m) at 12:30 LT (Fig. 3a) and at 18:30 LT (Fig. 3b). The vertical wind (w, Figs. 3c and 3d) and the zonal wind (u, Figs. 3e and 3f) below 500 hPa are also shown.

3.2 Effects of the underlying surfaces and background wind on the boundary-layer turbulence

3.2.1 Performance of the LEM and the height of the boundary layer over homogeneous and heterogeneous surfaces

In order to inspect the performance of the LEM over the heterogeneously heated surfaces, the simulated virtual potential temperature (θ_v) over the lake patch/patches and outside were compared with the observations. In addition, by keeping the total surface heat flux into the modeled domain constant, the profiles of the simulated virtual potential temperature over the homogeneous and heterogeneous surfaces were

删除[zhangysh]: .

删除[zhangysh]: at the surface (600 hPa, ~4200 m, 10 m wind field, 2 m temperature field; Fig. 3a) at 12:30 LT and

删除[zhangysh]: f

删除[zhangysh]: f

删除[zhangysh]: **flows**

删除[zhangysh]:

删除[zhangysh]: **ly heated**

删除[zhangysh]: **ly heated**

compared in order to investigate the effects of surface heterogeneity on the structure of the boundary layer. The profiles of the kinematic heat flux for all of the runs were used to determine the height of the boundary layer. Figures 4a and 4b compare the simulated profiles of the virtual potential temperature over and outside of the lake patch with the corresponding observations (solid lines) over the grassland and the lake surfaces at different times. In order to account for the effects of the unrepresented large-scale forcing, the simulated horizontally averaged potential temperature, water vapor mixing ratio, and horizontal wind (u and v) were relaxed to those observed using the radiosondes with a 3 h (hour) interval during the simulation (Marsham et al., 2008; Huang et al., 2009). The time series of the kinetic energy (see Fig. S2 in supplement) indicates that the equilibration time of the model is approximately 3 hours.

删除[zhangysh]: at

删除[zhangysh]: f

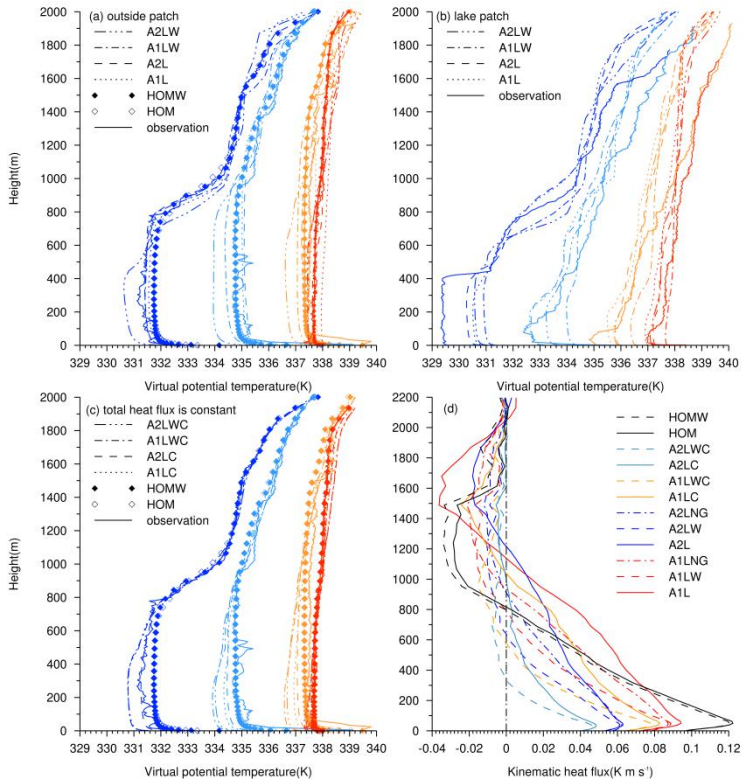

Figure 4. The profile of the horizontal, averaged virtual potential temperature for the observations and all of the runs over the lake patches (a) and outside of the lake patches (b). (c) same as (a) except, for heterogeneous and homogeneous runs with constant surface heat flux. Legends for (a), (b), and (c): dark and light blue represent the results at 09:30 and 12:30, respectively, and the orange and red lines show the results at 15:30 and 18:30, respectively. (d) The kinematic heat flux for all of the runs.

The observation profiles (solid lines in Fig. 4a) show that the depth of the convective boundary layer (CBL) over the grassland increases from 700 m at 09:30 to 1.1 km at 12:30 to 1.5 km at 15:30 to 1.9 km at 18:30. The inversion layer above the CBL is completely eroded by the turbulence after 12:30. The virtual potential temperature in the well-mixed CBL over the grassland increases approximately 7 K from 09:30 to 18:30. The CBL over the heterogeneous surfaces with background wind is cooler and shallower than that over the homogeneous surfaces. This may be because the background wind weakens the boundary-layer convection, which inhibits the development of the CBL (Huang et al., 2009). In addition, the model profiles of the virtual potential temperatures over the homogeneously heated and heterogeneously heated surfaces with no background wind have very similar structures and are close to the sounding profiles. This is similar to the modeling results of Liu et al. (2011). The observed virtual potential temperature over the lake surface (solid lines in Fig. 4b) shows that the CBL changes to stable stratification as the radiation increases after sunrise, and the modeled θ_v over the patches is about 1.0 K warmer than the observed θ_v. As in Fig. 4a, Fig. 4c also shows that the background wind over the heterogeneous surface inhibits the growth of the CBL.

In this study, according to Sullivan et al. (1998), the height of the boundary layer (z_i)

删除[zhangysh]: .
删除[zhanysh]: the
删除[zhanysh]: (b)
删除[zhangysh]: es
删除[zhangysh]: es
删除[zhangysh]: f
设置格式[zhangysh]: 字体: 小四, 非突出显示
删除[zhangysh]: the air blowing from the lake patches cools the CBL of the outside patches that are downwind, which inhibits the development of the CBL.
删除[zhangysh]: f
删除[zhangysh]: f
删除[zhangysh]: f
设置格式[zhangysh]: 下标

was determined using the minimum kinematic heat flux of the simulated results. As can be seen, the maximum surface heat flux were relatively large over the homogeneously heated surface, while smaller surface heat flux occurred for the case with two lake patches. Compared to the unbalanced cases (A1L, A1LW, A2L, and A2LW), less heat flux was introduced in the balanced cases (A1LC, A1LWC, A2LC, and A2LWC) and lower CBLs occurred, especially with a wind field (blue bars in Fig. 5). The kinematic heat flux decreased to zero at higher altitude over the heterogeneously heated surface. The region of negative heat flux above that altitude is often called the entrainment layer, which is thicker in the cases with background wind. The heights of the CBL indicate (Fig. 5) that the surface heat flux anomaly may contribute to the deepening of the mixed layer, thus increasing the CBL height. However, the shear generated by the background wind strengthens the turbulent exchange between the entrainment layer and the free atmosphere, resulting in an excessively thick entrainment layer, which, however, inhibits the upward development of CBL.

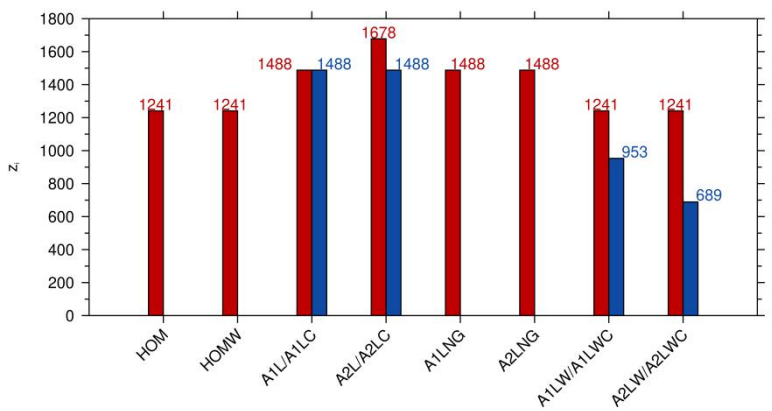

Figure 5. Bar chart of the CBL height for each run marked with a concrete value. The red bars from left to right represent runs HOM, HOMW, A1L, A2L, A1LNG, A2LNG, A1LW, and A2LW. The blue bars from left to right represent runs A1LC, A2LC, A1LWC, and A2LWC.

删除[zhangysh]: es
删除[zhangysh]: es
删除[zhangysh]: A1L_C
删除[zhangysh]: A1LW_C
删除[zhangysh]: A2L_C
删除[zhangysh]: A2LW_C
删除[zhangysh]: f
删除[zhangysh]: es
删除[zhangysh]: When the height continues to rise, t
删除[zhangysh]: .
删除[zhangysh]: A1L_C
删除[zhangysh]: A2L_C
删除[zhangysh]: A1LW_C
删除[zhangysh]: A2LW_C

3.2.2 Effects of the surface heat flux anomalies and background wind on the turbulent kinetic energy

Local circulations will be induced by differential heating, and the turbulent kinetic energy (TKE) determines the transport of the momentum, heat, and moisture through the boundary layer (Tyagi and Satyanarayana, 2013). Thus, the thermal circulations induced by the lake patches were simulated to investigate the effects of the heterogeneous heating on the spatial distribution of the TKE.

Fig. 6 shows the vertical distribution of the TKE and the wind vectors over the homogeneous and heterogeneous surfaces with and without background wind at 15:30 LT. Over the homogeneous surface (Fig. 6a), a relatively uniform TKE with a larger magnitude exists within a much shallower CBL (below 0.1 z_i), which overlies the scattered and disordered wind vectors throughout the domain. Over the heterogeneous surfaces, the large TKE values are distributed on both sides of the lake patches below 0.5 z_i, and the divergent winds extend to about 30 km away. In addition, a larger TKE and convergent winds occurred in the upper level of the CBL (Figs. 6b, 6c). Moreover, the air flow between the two lake patches led to a convergent region (updrafts in y= 0 km; Fig. 6c). This is consistent with the results of Avissar and Schmidt (1998), who demonstrated that turbulent eddies are randomly distributed over a homogeneous surface, but the TKE exhibits two maxima near the ground surface and the top of the CBL, which is in agreement with the patch-induced circulations. The similar TKE distribution occurs when the background wind exists over the homogeneous surface (Figs. 6a and 6d). It should be noted that there is larger TKE over the patch/patches

删除[zhangysh]: s

删除[zhangysh]: no

设置格式[zhangysh]: 下标

设置格式[zhangysh]: 下标

(below 0.2 z_i) as the similar pattern of TKE in Papangelis et al. (2021), from which the TIBL can be recognized (Figs. 6e and 6f). Moreover, the background wind inhibits the development of the patch-induced circulation because the divergent wind derived from the heterogeneous surface can not be viewed at 15:30. Overall, Figure 6 illustrates that the distributions of the TKE and the patch-induced circulations are symmetrical on both sides of the lake patches, while the distribution is random with smaller TKE values over the homogeneous surface. The background wind tends to reduce the TKE outside patch/patches while enhance it over the patch/patches.

Furthermore, the ratios of the horizontally averaged TKE in the model domain of the different runs were calculated to examine the effects of the surface anomalies and the background wind on the TKE. As is shown in Table 2, the TKE for the cases with one or two lake patches are about twice that of the TKE of the case without patches (columns 2–3), but the background wind leads to a reduction in the impacts of surface flux heterogeneity on the TKE (columns 4–5 and 6–7). This is consistent with the results of Avissar and Schmidt (1998), who reported that a weak background wind of 2.5 m/s is strong enough to considerably reduce the impact of the surface heterogeneity on the CBL. For the homogeneous cases, the TKE increases under the background wind conditions due to the increase in the sheared turbulence. For the runs with balanced surface heat flux (A1LC, A2LC, A1LWC, A2LWC), the effects of the heterogeneity on the TKE are less significant due to the relative smaller surface heat flux, especially for the cases with more lake patches, but the effects of the background wind on the TKE tend to be large.

删除[zhangysh]: s

删除[zhangysh]: ambient winds

删除[zhangysh]: s

删除[zhangysh]: ambient

删除[zhangysh]: ground-

删除[zhangysh]: es

删除[zhangysh]: A1L_C

删除[zhangysh]: A2L_C

删除[zhangysh]: A1LW_C

删除[zhangysh]: A2LW_C

删除[zhangysh]: s

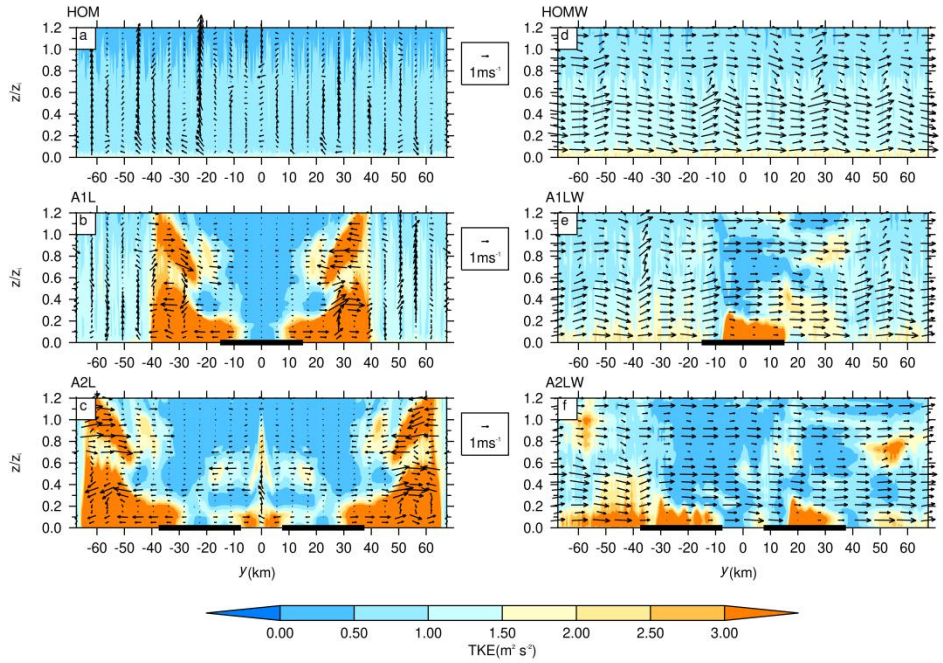

388 **Figure 6.** The y-z cross sections of the TKE (contour) with superimposed wind vectors composed
389 of *v* and *w* wind for runs with (d, e, f) and without (a, b, c) background wind over homogeneous (a,
390 d) and heterogeneous (b, e and c, f) surfaces. The thick black lines on the y-axis represent the lake
391 patches.

392 **Table 2**

393 The ratio of the TKEs of the different runs. Max, Min, and Mean stand for the maximum,
394 minimum, and mean ratios of the TKE in the model domain, respectively.

Ratio of TKE	A1L/HOM	A2L/HOM	A1LW/HOMW	A2LW/HOMW	A1LW/A1L	A2LW/A2L	HOMW/HOM
Max	3.31	3.30	1.47	1.42	1.01	0.88	2.09
Min	1.15	1.18	0.80	0.59	0.61	0.40	0.83
Mean	2.00	2.04	1.09	0.95	0.79	0.68	1.41
Ratio of TKE	A1L/HOM	A2L/HOM	A1LW/HOMW	A2LW/HOMW	A1LW/A1L	A2LW/A2L	HOMW/HOM
Max	2.21	1.44	1.12	0.74	1.84	2.17	2.09
Min	0.43	0.23	0.63	0.31	0.80	0.47	0.83
Mean	1.09	0.75	0.91	0.54	1.22	1.07	1.41

395 To further investigate the effects of the surface heat flux anomalies on the
396 development of turbulence, it is instructive to examine the vertical profiles of the
397 buoyancy and shear production terms in the TKE budget equation, which is from the

删除[zhangysh]: .

删除[zhangysh]: over (a) homogeneously heated and (b and c) heterogeneously heated surfaces.

删除[zhangysh]: blue

带格式表格[zhangysh]

删除[zhangysh]:

删除[zhangysh]:

删除[zhangysh]:

删除[zhangysh]:

删除[zhangysh]:

删除[zhangysh]:

删除[zhangysh]:

删除[zhangysh]:

398 contributions of the resolved (RES) and subgrid (SGS) eddies at 15:30 LT (Figs. 7a,

399 7b, and 7c).

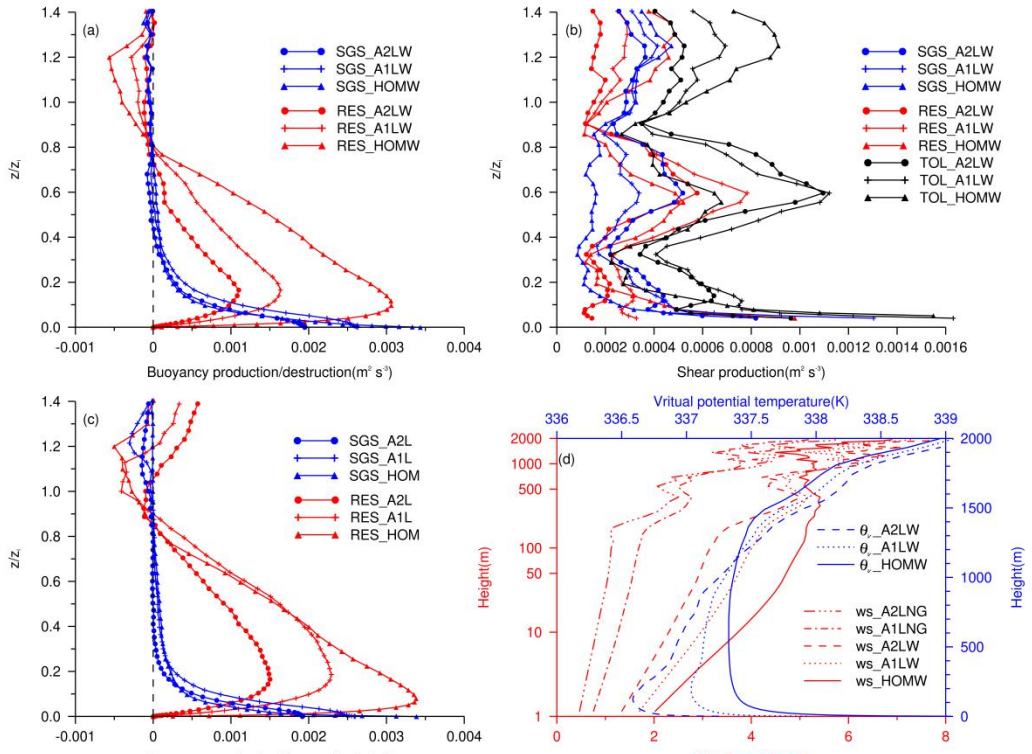

400 **Figure 7.** Vertical profiles of the buoyancy flux (a) and the shear production term (b) for runs

401 HOMW, A1LW, and A2LW with background wind, and the profiles of the buoyancy flux (c) for

402 runs HOM, A1L, and A2L without background wind. (d) The simulated mean wind versus

403 logarithm of height for runs HOMW, A1LW, A2LW, A1LNG and A2LNG, and the virtual

404 potential temperature profiles (blue line) at the same time (15:30 LT). The resolved and subgrid

405 results are presented as red and blue lines, respectively. The black lines in (b) are the total

406 (resolved and subgrid scale) shear production term.

407 Figures 7a and 7c show that the RES buoyancy production/destruction decreases as

408 the number of patches increases and the SGS buoyancy contributions are negligible,

409 except in the surface layer. The buoyancy production/destruction in the TKE budget

410 equation is $B = \frac{g}{\theta_v} \overline{w'\theta_v'}$. The RES buoyancy production/destruction profiles show

411 that the lower maximum occurs for the wind simulations over the heterogeneous

删除[zhangysh]: .

删除[zhangysh]: (a)

删除[zhangysh]: (b)

删除[zhangysh]: flows

删除[zhangysh]: (c)

删除[zhangysh]: flows

删除[zhangysh]: horizontal

删除[zhangysh]: and

设置格式[zhangysh]: 非突出显示, 字距调整: 1 磅

设置格式[zhangysh]: 非突出显示, 字距调整: 1 磅

设置格式[zhangysh]: 非突出显示, 字距调整: 1 磅

删除[zhangysh]: yellow and purple

surfaces. It is because the larger positive buoyancy production/destruction decreases, especially in the downstream of the patch (Fig. S4 in the supplement), which is due to the significantly weakened updrafts of the patch-induced circulations by the background wind. Comparing with no wind simulations (Figs. S4b, S4c), the buoyancy production/destruction over the patch/patches decreases for wind simulations. It is probably caused by the relatively warm air in a thermal internal boundary layer (TIBL) formed over the patch/patches (Figs. S5b, S5c) due to the abrupt change in surface heat flux (Mahrt, 2000) with air flowing from the warm patch to the cold patch. Similar with the results of Zhou et al. (2018) and Liu et al. (2020), the cold center of the TIBL (Figs. S5e, S5f) moves to the downwind of the lake patches. Below 0.9 z_i, the larger RES shear production occurs in the case with lake patches (Fig. 7b) and the contribution of the SGS shear production is considerable (Fig. 7b), which is significant in the CBL for the cases with surface flux anomalies. Thus, the total shear productions (black lines in Fig. 7b) of the cases with heterogeneous surfaces are larger. In addition, wind shear is the source of the SGS shear production peak at z/z_i = 0.6 due to the larger momentum flux above 0.6 z_i (see Fig. S3) increasing the wind speed and wind shear below. Fig. 7d showed the wind profiles (red lines) for runs with background wind (HOMW, A1LW, A2LW) and without geostrophic wind (A1LNG, A2LNG), and the virtual potential temperature profiles (blue lines). It shows that patch-induced circulations reduce the modeled mean wind speed below the height of about 800 m, for the largest wind speed exists in the homogeneous case (red solid line). The wind profile is log-linear below the height

设置格式[zhangysh]: 下标

删除[zhangysh]: f

of 20 m and shows a clear mixed layer above it for the homogeneous run, which correspond to a mixed layer shown by the virtual potential temperature profile (blue solid line). For the one/two-lake simulations, the wind profiles (red dotted and dashed lines) exhibit a feature of a stable boundary layer (blue dotted and dashed lines) with a maximum local wind at about 400 m. It should be noted that the stable stratification of wind profiles between 200 m and 1000 m are probably caused by the process of the TIBL. It is confirmed by the similar wind profile features from the runs without geostrophic wind over the heterogeneous surface.

3.2.3 Effects of the background wind on the circulations

In order to investigate the effects of the background wind on the patch-induced circulations, the vertical distributions of the vertical velocity and wind fields for the runs with and without background wind were compared. In Fig. 8, the patch-induced circulations are not easy to distinguish in the cases with background wind (about 13.9 $m \cdot s^{-1}$ above a height of 1.2 km) due to the cancellation of the local pressure gradient by the synoptic pressure gradient, which is consistent with the results of Crosman and Horel (2010). This also indicates that the boundary-layer convection tends to weaken as the number of lake patches increases (the maximum updrafts are 4.8 $m \cdot s^{-1}$, 4.2 $m \cdot s^{-1}$, 3.5 $m \cdot s^{-1}$, and 3.3 $m \cdot s^{-1}$ for runs A1L, A2L, A1LW, and A2LW, respectively), which is confirmed by the weaker buoyancy production/destruction for the heterogeneous simulations in the Figs. 7a and 7c. Moreover, the wind fields for the cases without geostrophic winds exhibit divergent flows over the lake patches. As in the study of Kang and Lenschow (2014), our study also confirms that the symmetrical

删除[zhangysh]: The background winds (Fig. 7d) are weaker for the cases with lake patches below 0.65 z_i, but the corresponding total shear production term is larger, which shows that the patch-induced circulations are conducive to more shear in the CBL.

设置格式[zhangysh]: 下标

删除[zhangysh]: **flows**

删除[zhangysh]: s

删除[zhangysh]: s

删除[zhangysh]: f

删除[zhangysh]: s

删除[zhangysh]: m/s

设置格式[zhangysh]: 上标

patch-induced circulations and the intensity of the convection become indistinguishable and weak under the background wind conditions. However, the divergent flows in the lower level are still visible when the geostrophic wind is removed (A1LNG and A2LNG in Figs. 8e and 8f). Comparing with the spatial distribution of the vertical velocity over the homogeneous surface (Figs. 8g and 8h), the lake patch/patches alters both the boundary-layer convection intensity and the local circulation.

删除[zhanysh]: flow

删除[zhangysh]: f

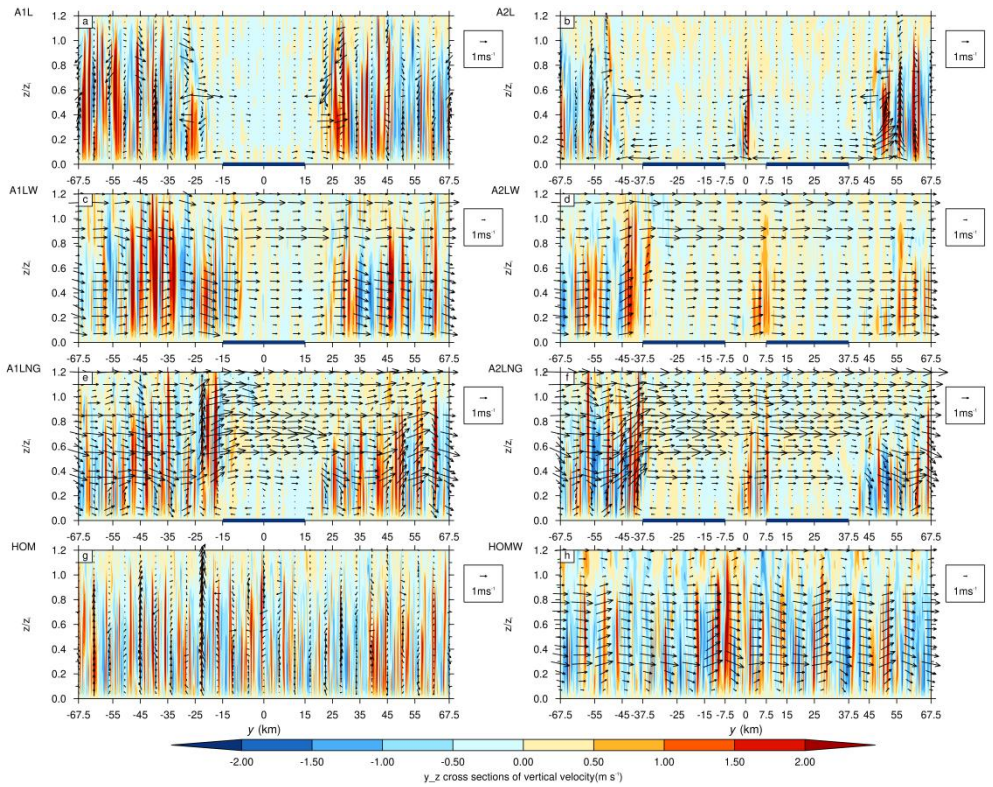

Figure 8. Instantaneous y-z cross sections of the vertical velocity ($m \cdot s^{-1}$) and wind vectors above the heterogeneous surfaces for runs without (a and b) and with (c and d) background wind, and with the geostrophic wind removed (e and f), as well as the results over homogeneous surfaces for runs with (h) and without (g) background wind. The blue lines represent the lake patches.

删除[zhangysh]: .

删除[zhangysh]: (a and b)

删除[zhangysh]: (c and d)

删除[zhangysh]: s

删除[zhangysh]: (e and f)

3.3 Effects of patch-induced circulation on the turbulent intensity and heat flux

We used the phase-averaged method to decompose the contributions of the turbulent intensity and the heat flux from the patch-induced circulations and the background turbulence and to quantitatively analyze the heterogeneity-induced contribution to the turbulent intensity. For the variance of the velocity, the horizontal (Fig. 9a) and vertical (Fig. 9b) variances induced by the heterogeneity increase as the number of lake patches increases, and the horizontal variance is larger than the vertical variance. However, the background wind tends to decrease both the patch-induced (Figs. 9a, 9b) and total (Figs 9e, 9f) turbulent intensity.

删除[zhangysh]: flows

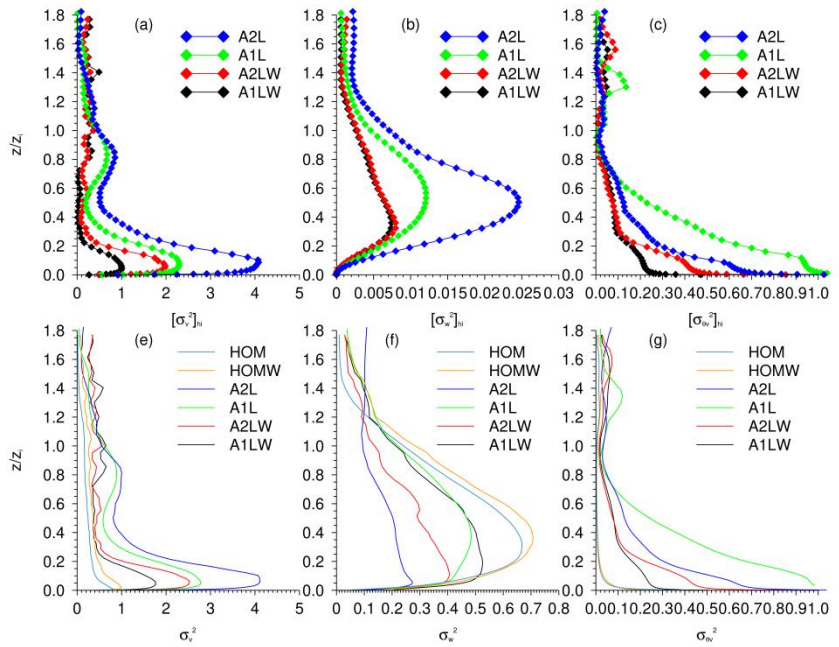

Figure 9. Heterogeneity-induced (a, b, c) and total (e, f, g) dimensionless turbulence statistics for runs HOM, HOMW, A1L, A1LW, A2L, and A2LW. Shown are the profiles of the (a, e) *v* variance, (b, f) *w* variance, and (c, g) θ variance.

删除[zhangysh]: .

删除[zhangysh]: (a, b, c)

删除[zhangysh]: (e, f, g)

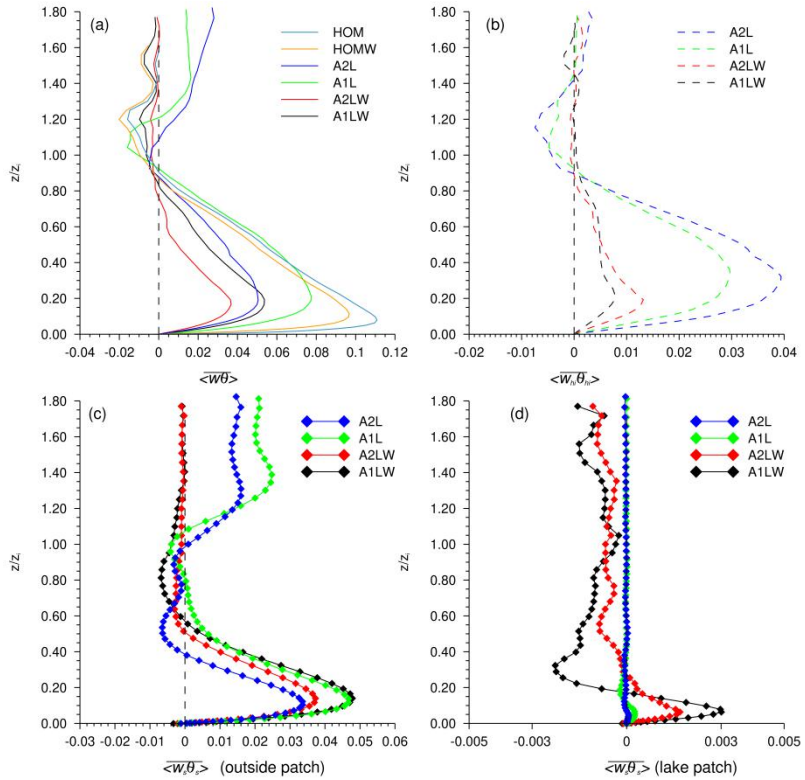

480 **Figure 10.** (a) Area-averaged total turbulent heat flux (solid lines) and (b) heterogeneity-induced

481 turbulent heat flux (dash lines). The background turbulence (lines with diamond symbols) of heat

482 flux over the grassland (c) and lake patches (d).

删除[zhangysh]: .

删除[zhangysh]: (c)

删除[zhangysh]: (d)

483 This also shows that a larger difference in the variances of the horizontal velocity

484 occurs in the surface layer and gradually decreases with height (Figs. 9a and 9e),

485 which means that the effects of the surface properties on the horizontal turbulence

486 diminish with height in the CBL. In this respect, our results are similar to those found

487 by Wang et al. (2011), Shao et al. (2013), and Frederik and Matthias (2018). The total

488 horizontal turbulent intensity is mainly from the contribution of the patch-induced

489 circulations and is larger than that of the homogeneous cases (Fig. 9e), which tends to

490 become stronger as the number of patches increases but becomes weaker as the total

491 vertical turbulent intensity increases (Fig. 9f, same as in the cases with balanced

492 surface fluxes). It should be noted that the contribution of the patch-induced

493 circulations to the vertical velocity variance is no more than 10% (Fig. 9b and 9f),
494 which implies that the background turbulence contributes more to the fluctuations in
495 the vertical velocity than to those in the horizontal velocity. Figures 9c and 9g show
496 that the patch-induced motions make the largest contribution to the variances of the
497 potential temperature. However, the background wind decreases the variances of the
498 potential temperature and decrease the impact of the surface heterogeneity on the
499 variances of the potential temperature.

500 Using the same method, we analyzed the contributions of the patch-induced and
501 background turbulence to the heat flux. Figure 10a shows that as the number of lake
502 patches increases, the area-averaged total heat flux decreases in both the mixed and
503 entrainment layers, and the balanced surface heat flux cases exhibit similar variations
504 (see Fig. S6 in supplement). The patch-induced transport of the heat flux increases as
505 the number of lake patches increases (Fig. 10b). The patch-induced motions
506 contribute up to 80% of the heat flux in run A2L, which has unbalanced surface fluxes
507 (Fig. 10b), and 61% in run A2LC which has balanced surface fluxes (see Fig. S6 in
508 supplement). It should also be noted that the background wind tends to decrease the
509 heat flux transport over the heterogeneous surfaces. As is shown in Figs. 10c and 10e,
510 the contribution of the background turbulence to the local heat flux is larger over the
511 region outside of the lake patches than over the patches. Notice that the minimum heat
512 flux (Fig. 10d, at about 0.3 z_i) is in the magnitude so strong as it is close to the surface
513 (0.1 z_i). It probably contributes the local maximum wind speed. We hope that the
514 results of our analysis of the contributions of the heterogeneity-induced circulation

删除[zhangysh]: s
删除[zhangysh]: fig.03
删除[zhangysh]: A2L_C
删除[zhangysh]: fig. S3
删除[zhangysh]: s
删除[zhangysh]: f

and background turbulence to the turbulence intensity and the heat flux over a heterogeneous surface will provide a basis for further studies of the local energy and mass transport in the SRYR over the TP.

3.4 Turbulence in the surface layer

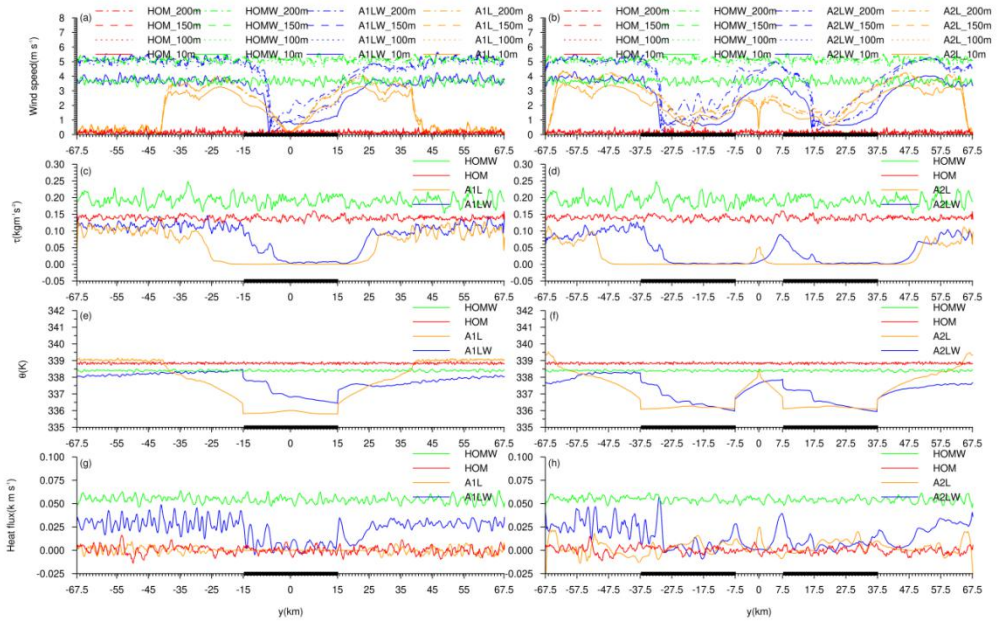

Figure 11. Variations in the wind speed (a and b) and Reynolds stress (c and d), potential temperature (e and f) and heat flux (g and h) in the horizontal direction below 200 m for the cases with (blue and green lines) and without (yellow and red lines) background wind over homogeneous (red and green lines) and heterogeneous (blue and yellow lines) surfaces. Thick black lines represent the lake patches.

The frictional velocity (u_*) is a critical parameter in the turbulence exchange near the surface, and it plays an important role in the transport of momentum in the boundary layer. Patil et al. (2016) reported that the frictional velocity increases with wind speed under lower wind speed conditions in the surface layer. Thus, we focused on the variations in the wind speed (Figs. 11a and 11b) and Reynolds stress (Figs. 11c and 11d) in the horizontal direction below 200 m in order to investigate the effects of

删除[zhangysh]: .
删除[zhangysh]: (a and b)
删除[zhangysh]: (c and d)
删除[zhangysh]: flows
设置格式[zhangysh]: 非突出显示
删除[zhangysh]: increasing

the patch-induced motions on the momentum flux in the surface layer for various background wind. It was found that the inland extension of the patch-induced divergent flows reached about 25 km with no background wind (yellow curves in Figs. 11a and 11b). The speed of the divergent winds increases from the lake patches to the outside and increases with height below 200 m with and without background wind. The wind speeds decrease rapidly (4.0 m : s^{-1}) within 10 km along with the wind blowing from west of the lake patches to east of the lake patch, and then, the wind speeds increase steadily (blue curves in Figs. 11a and 11b). The changes in the surface winds and surface properties have significant effects on the turbulent momentum flux. Figures 11c and 11d show that the transport of the momentum flux is smaller over the heterogeneous surface. The consistent variations in the wind speeds and the turbulent stresses illustrate that the lake patches alter the spatial distribution of the turbulent stress, which would further affect the surface wind speeds, especially over the land-lake boundary regions. Moreover, the potential temperature (Figs. 11e, 11f) and the sensible heat flux (Figs. 11g, 11h) increase abruptly from the lake patch to the grass patch (e.g. from y=15 km to y=25 km in Fig. 11e), which indicates the formation of the TIBL.

删除[zhangysh]: s

删除[zhangysh]: s

删除[zhanysh]: f

删除[zhangysh]: s

删除[zhanysh]: f

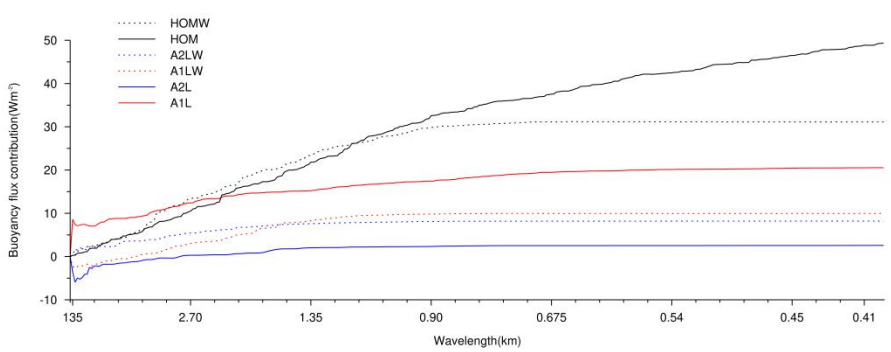

Figure 12. The cumulative contribution of the buoyancy flux of all wavelength (km) at a height of 50 m for runs HOM, HOMW, A1L, A2L, A1LW, and A2LW.

In order to quantify the contributions of the buoyancy fluxes, due to the different scales of the eddies, we calculated the ogives, which are the running integrals of the cospectral densities (Friehe et al., 1991), and used these values to show the cumulative contribution to the fluxes of all of the wavelengths (Brooks and Rogers, 2000). The ogives curves (Fig. 12) show that the small eddies make a significant contribution to the buoyancy fluxes over the homogeneous surfaces with no background wind (solid black line). The background wind increases the buoyancy flux for wavelengths larger than about 1.1 km and decreases it for smaller wavelengths based on a comparison of cases HOM (solid black line) and HOMW (black dotted line). The above results confirm that the heat transport is enhanced by the large eddies but is weakened by the small eddies, especially under the control of the background wind. The buoyancy flux for a wavelength larger than about 2.2 km makes a greater contribution in the case with one lake patch without background wind (solid red line). The buoyancy fluxes for wavelengths of greater than 2.7 km are transported downward for the case with two lake patches. For the case with one lake patch, the background wind tends to decrease the transport of the buoyancy flux for larger wavelengths near the surface (red dotted line) due to the stronger horizontal wind (Fig. 7d), and they help to transport the buoyancy fluxes downward for wavelengths larger than 3.3 km. However, for the case with two lake patches, the background wind causes the large eddies to transport the buoyancy fluxes upward. Thus, increasing the number of lake patches leads to more patch-induced motions, but

删除[zhangysh]: .
删除[zhangysh]: es
删除[zhangysh]: s
删除[zhangysh]: s
删除[zhangysh]: s
删除[zhangysh]: flows

570 this does not tend to enhance the ability of the wind to transport heat. It is concluded
571 that slightly more of the buoyancy flux of the case with one lake patch is transported
572 by the small eddies with wavelengths of less than 1.5 km compared with the case with
573 two lake patches and background wind conditions (red and blue dotted lines).

574 **3.5 The characteristics of the boundary-layer turbulence in the**
575 **entrainment layer**

576 The LES study conducted by Matthias et al. (2014) found that there is increased
577 entrainment from the more strongly heated surface patch cases compared to the
578 homogeneous cases, and the impact of the heterogeneity on entrainment vanishes due
579 to horizontal mixing if the mean flow is aligned perpendicular to the border between
580 the differentially heated patches. To investigate the effects of the thermal properties of
581 the heterogeneous surface and the background wind on the turbulence in the
582 entrainment layer, the characteristics of the heat flux in the entrainment layer were
583 analyzed. Our simulated results show that the downward transport of the heat flux
584 decreases as the number of lake patches increases in the entrainment layer for both the
585 wind and no wind cases (Figs. 4d and 10a), which is also true in the balanced heat
586 flux runs.

587 By comparing the maximum and minimum vertical velocities at the top of the
588 boundary layer (Table 3), we found that the convective intensity of the entrainment
589 layer in the case with two lake patches and no wind fields is stronger, but it is
590 weakened by the background wind. Whereas, it decreases as the number of lake
591 patches increases in the balanced heat flux cases (A1LC and A2LC), corresponding to

删除[zhangysh]: flows

删除[zhangysh]: flows

删除[zhangysh]: A1L_C

删除[zhangysh]: A2L_C

592 a smaller TKE (Table 2) and total turbulent intensity (Fig. 9f). Huang et al. (2009)
593 pointed out that an appropriate surface heat flux and background wind maintain the
594 convective roll, and our simulations demonstrate this roll-like convection (see Fig. S7
595 in supplement), which is mainly induced by the persistence of the background
596 turbulence with stronger geostrophic winds of 7–11 m·s^{-1} (black lines in Fig. 2g).
597 However, Maronga and Raasch (2013) found that a higher wind speed of 6 m·s^{-1}
598 generates convective rolls derived from the secondary circulation over a complex
599 heterogeneous surface.

删除[zhangysh]: 7

删除[zhangysh]: flows

删除[zhangysh]: fig. S4

删除[zhangysh]: f

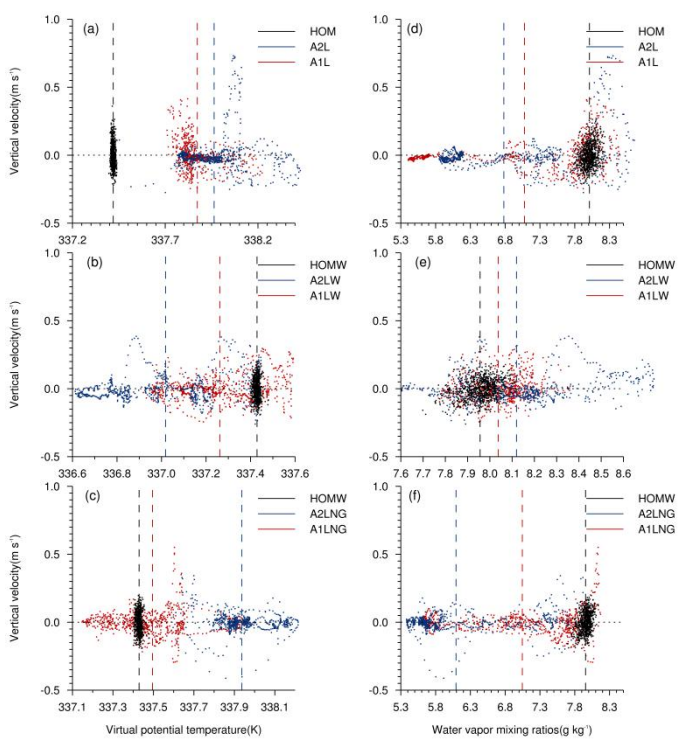

600 **Figure 13.** The joint vertical velocities, virtual potential temperatures (a, b, c) and water vapor
601 mixing ratios (d, e, f) at the top of the CBL for the homogeneous runs (black dot) and
602 heterogeneous runs (red for one-lake and blue for two-lakes). The black dotted lines represent the
603 mean vertical velocity, the black, red and blue dashed lines show the mean virtual potential
604 temperatures and water vapor mixing ratios for the homogeneous, one-lake and two-lakes runs,
605 respectively.

删除[zhangysh]: .

删除[zhanysh]: (a, b, c, d, e, f)

删除[zhanysh]: and

删除[zhanysh]: (g, h, i, j, k, l)

删除[zhanysh]: and

删除[zhanysh]: and

In addition, the boundary layer variables (including the vertical velocities, virtual potential temperatures, and water vapor mixing ratios) in the entrainment layer are also subject to the effects of the surface heterogeneity. Figure 13 shows the joint distribution of the vertical velocities and the virtual potential temperatures, as well as the vertical velocities and water vapor mixing ratios. Comparing to the homogeneously heated cases, the increased downdrafts mainly occur over the lake patches, and they carry more warm, dry air down from the free atmosphere (Figs. 13a, 13b, 13g, and 13h), which is due to the convergent airflow caused by the patch-induced circulations at the top of the CBL. This effect is much more evident in the case with two lake patches, but it is weakened by the gradually strengthening background wind (except Figs. 13a, 13b, 13g, and 13h). We obtained the same results for the balanced cases. In particular, colder and moister air exists in the entrainment layer in the cases with background wind (A1LWC and A2LWC).

删除[zhangysh]: flows

删除[zhangysh]: f

删除[zhangysh]: ambient winds

删除[zhangysh]: A1LW_C

删除[zhangysh]: A2LW_C

Table 3

The maximum and minimum vertical velocities at the top of the boundary layer in cases A1LW, A2LW, A1LWC, A2LWC, A1LNG, A2LNG, A1L, A2L, A1LC, A2LC and HOM, HOMW.

删除[zhanysh]: A1LW_C

删除[zhanysh]: A2LW_C

Case	A1LW	A2LW	A1L	A2L	HOM	HOMW
W(max)	4.01	3.54	5.42	5.55	4.37	4.48
W(min)	−2.29	−1.98	−2.40	−3.12	−2.15	−2.50
Case	A1LWC	A2LWC	A1LC	A2LC	A1LNG	A2LNG
W(max)	2.97	2.06	4.26	2.46	3.90	4.46
W(min)	−2.03	−1.25	−1.91	−1.27	−2.23	−1.97

删除[zhanysh]:

删除[zhanysh]:

删除[zhanysh]:

删除[zhanysh]:

4 Summary and discussion

The downdrafts and divergent zonal wind in the two lakes area obtained from the ERA-Interim reanalysis data indicate the existence of a lake breeze in the SRYR. Ten

runs of the 1D strip-like distribution of the surface heat flux and two homogeneous runs based on the observations made during the summer of 2012 in the Ngoring Lake Basin were conducted in order to investigate the effects of the patch-induced circulations on the boundary-layer turbulence and its energy transport at the lake-air and grass-air interfaces, and the influence of the background wind also be considered.

The thermodynamic heterogeneity of the surface is conducive to deepening the mixed layer, thus increasing the CBL height and enhancing the TKE when there are no background wind. The background wind brings shear, resulting in an excessively thick entrainment layer, which inhibits the growth of CBL and reduce the effects of the heterogeneous surface on the TKE. The distribution of the TKE over the heterogeneous surface is consistent with the patch-induced circulations described by Avissar and Schmidt (1998). In addition, the enhanced effects by surface heat anomoly on the TKE are far lower in the cases with an balanced surface heat flux. By analyzing the buoyancy and shear production terms in the TKE budget equation and separating the contribution of the resolvable-scale (RES) and subgrid-scale (SGS) eddies, we found that the contributions of the wind shear to the TKE from the SGS eddies are considerable in the CBL (below 0.9 z_i) over a heterogeneous surface. The patch-induced circulations reduce the modeled mean wind speed. The clear mixed layer is shown by the wind and virtual potential temperature profiles for the homogeneous run, while the stable stratification of wind profiles for the heterogeneous simulations are probably caused by the process of the TIBL. We obtained the same conclusion as Kang and Lenschow (2014), that is, the

删除[zhangysh]: ly

删除[zhangysh]: heated

删除[zhangysh]: flows

删除[zhangysh]: flows

删除[zhangysh]: flows

删除[zhangysh]: ly heated

删除[zhangysh]: ly heated

删除[zhangysh]: the surface heat anomaly and background winds have similar effects on the CBL in the cases with a balanced surface heat flux, but

删除[zhangysh]: un

删除[zhangysh]: Thus, it is more beneficial to consider the ambient winds.

设置格式[zhangysh]: 下标

删除[zhangysh]: ly heated

删除[zhangysh]: The total shear production term is larger below 0.65z_i in the heterogeneously heated cases with weaker background winds, demonstrating that the patch-induced circulations are conducive to producing more shear in the CBL.

设置格式[zhangysh]: 下标

patch-induced circulations become indistinguishable under background wind conditions, and the background wind also weakens the convective intensity.

Then, we conducted a phase-averaged analysis to separate the contributions of the turbulent intensity and the transport of the total heat flux from those of the patch-induced circulations and the background turbulence field. The patch-induced turbulent intensity increases with increasing lake patches. It mainly contributes to the horizontal turbulent intensity and the potential temperature variance, while it contributes no more than 10% to the vertical turbulent intensity, of which the background turbulence contributes the most. The background wind weakens the patch-induced and horizontal turbulent intensities but strengthen the vertical turbulent intensity. The contribution of the patch-induced heat flux was up to 80% in the unbalanced cases and 60% in the balanced cases. The background turbulence made a larger contribution to the heat flux over the outside of patches, which have a stronger surface heat flux than that over the lake patches. The background wind also inhibits the transport of the heat flux.

To understand the effects of the patch-induced motions on the momentum flux in the surface layer under various background wind conditions, we focused on the variations in the wind speed and the Reynolds stress in the horizontal direction below 200 m. Without background wind, the inland extent of the patch-induced flows was about 25 km. When the background wind flowed into the lake patches, they decreased by 4.0 $m \cdot s^{-1}$ within about 10 km and increased steadily when flowing out of the patches. The synchronized variations in the wind speed and momentum flux in the

删除[zhangysh]: flows
删除[zhangysh]: ambient
删除[zhangysh]: s
删除[zhangysh]: ambient
删除[zhangysh]: s
删除[zhangysh]: area
删除[zhangysh]: the
删除[zhangysh]: flows
删除[zhangysh]: ambient
删除[zhangysh]: s
删除[zhangysh]: s

669 horizontal direction illustrate that the lake patches alter the spatial distribution of the
670 turbulent stress, which further affects the surface wind speeds, especially over the
671 land-lake boundary regions. We also analyzed the cumulative contribution of eddies
672 with different scales to the buoyancy flux near the surface. It was found that without
673 background wind, the buoyancy flux is transmitted upward by the eddies with larger
674 wavelengths for the case with one lake patch; while there is a negative buoyancy flux
675 in the case with two lake patches. Thus, increasing the number of lake patches leads
676 to more patch-induced motions, which do not tend to enhance the heat transport
677 ability. The background wind promotes the opposite results.
678 In the entrainment layer, in contrast to Matthias et al. (2014) who found that the
679 entrainment increased for the stronger heated surface patch cases compared to the
680 homogeneous case, we found that the entrainment flux decrease as the number of lake
681 patches increases. For the unbalanced cases, the convective intensity increases as the
682 number of lake patches increases, but the background wind weakens it. For the
683 balanced cases, the convective intensity weakens as the number of lake patches
684 increases, corresponding to a smaller TKE and total turbulent intensity. In this study,
685 whether the convective rolls persist mainly depended on the background turbulence
686 field with a higher geostrophic wind of 7–11 $m \cdot s^{-1}$, while Maronga and Raasch (2013)
687 reported a higher wind speed of 6 $m \cdot s^{-1}$. As the number of lake patches increases, the
688 increased downdrafts are mainly located over the lake patches, and they carry more
689 warm, dry air down from the free atmosphere in both the balanced and unbalanced
690 cases. The background wind weakens this effect even when there is cooler, moister air

删除[zhangysh]: flows

删除[zhangysh]: flows

删除[zhangysh]: flows

删除[zhangysh]: s

in the entrainment layer in the balanced cases.

Our study provides ideal simulations of the boundary-layer turbulence over the heterogeneous surface in the SRYR. It mainly focused on the influences of the heterogeneous distribution of the surface heat flux and the background wind. In the future, we plan to conduct further research that will take into consideration the topography and additional physical processes to provide a reference for the study of the energy and water exchange processes over the complex surface of the SRYR.

Data availability. The data presented in the paper can be accessed via contacting Yunshuai Zhang (zhangysh13@lzu.edu.cn).

Code availability. The code can be accessed via contacting Yunshuai Zhang (zhangysh13@lzu.edu.cn).

Author contributions. QH and YM had the original idea of the study. CW and ZL provided the observation data. YZ and YC conducted model simulation. YZ and YC interpreted the data and plotted the figures. YZ wrote the manuscript with contributions from all the co-authors.

Competing interests. The authors declare that they have no conflict of interest.

Acknowledgments. Thanks to the Zoige Plateau Wetland Ecosystem Research Station, Chinese Academy of Sciences for the field observation data, it supported by the

删除[zhangysh]: ly heated

删除[zhangysh]: s

设置格式[zhangysh]: 字体: 非加粗, 倾斜

设置格式[zhangysh]: 字体: 非加粗

设置格式[zhangysh]: 字体: 非加粗

设置格式[zhangysh]: 字体: 非加粗

设置格式[zhangysh]: 字体: 非加粗

设置格式[zhangysh]: 字体: 非加粗

设置格式[zhangysh]: 字体: 非加粗

设置格式[zhangysh]: 字体: 倾斜

设置格式[zhangysh]: 字体: 倾斜

设置格式[zhangysh]: 字体: 非加粗

Science and Technology Plan of Gansu Province (20JR10RA070). We also thank the three anonymous reviewers for helpful comments during ACP discussions.

Financial support. This research was supported by the second Tibetan Plateau Scientific Expedition and Research Program (STEP, 2019QZKK0604, 2019QZKK0103), the National Natural Science Foundation of China (NSFC) (41775013, 91837208).

Review statement. This paper was edited by Stefano Galmarini and reviewed by three anonymous referees.

设置格式[zhangysh]: 字体: 倾斜

References

Avissar, R., and Pielke, R. A.: A Parameterization of Heterogeneous Land Surfaces for Atmospheric Numerical Models and Its Impact on Regional Meteorology, Monthly Weather Review, 117(10), 2113-2136. doi:10.1175/1520-0493(1989)117<2113:APOHLS>2.0.CO;2, 1989.

Avissar, R., and Schmidt, T.: An Evaluation of the Scale at which Ground-Surface Heat Flux Patchiness Affects the Convective Boundary Layer Using Large-Eddy Simulations, Journal of the Atmospheric Sciences, 55(16), 2666 – 2689. doi:10.1175/1520-0469(1998)055<2666:AEOTSA>2.0.CO;2, 1998.

Ao, Y. H., Lyu, S. H., Li, Z. G., Wen, L. J., and Zhao, L.: Numerical simulation of the climate effect of high-altitude lakes on the Tibetan Plateau. Sciences in Cold and

删除[zhangysh]: **Acknowledgments**
This research was supported by the second Tibetan Plateau Scientific Expedition and Research Program (STEP, 2019QZKK0604), the National Natural Science Foundation of China (NSFC) (91837208, 41775013). Thanks to the Zoige Plateau Wetland Ecosystem Research Station, Chinese Academy of Sciences for the field observation data, it supported by the Science and Technology Plan of Gansu Province (20JR10RA070)

删除[zhangysh]:

728 Arid Regions, 10(5): 0379 – 0391. doi: 10.3724/SP.J.1226.2018.00379, 2018.
729 Biermann, T., Babel, W., Ma, W. Q., Chen, X. L., Thiem, E., Ma, Y. M., and Foken, T.:
730 Turbulent flux observations and modelling over a shallow lake and a wet
731 grassland in the Nam Co basin, Tibetan Plateau. *Theor. Appli. Clima.*, **116**,
732 301-316, doi: 10.1007/s00704-013-0953-6, 2014.
733 Brierley, G. J., Li, X., Cullum, C. and Gao, C. (Eds.): Landscape and Ecosystem
734 Diversity, Dynamics and Management in the Yellow River Source Zone,
735 Springer International Publishing, 2016.
736 Brooks, I. M., and Rogers, D. P.: Aircraft observations of the mean and turbulent
737 structure of a shallow boundary layer over the Persian Gulf [J]. Bound.-Layer
738 Meteor., 95(2): 189 – 210. doi:10.1023/A:1002623712237, 2000.
739 Brown, A. R., Derbyshire, S. H. and Mason, P. J.: Large-eddy simulation of stable
740 atmospheric boundary layers with a revised stochastic subgrid model. *Quart. J.*
741 *Roy. Meteor. Soc.*, 120(520), 1485-1512,
742 https://doi.org/10.1002/qj.49712052004, 1994.
743 Chen, X., Añel, J. A., Su, Z. B., Torre, L. D. L., Kelder, H., Peet, J. V., and Ma, Y. M.,
744 The Deep Atmospheric Boundary Layer and Its Significance to the Stratosphere
745 and Troposphere Exchange over the Tibetan Plateau. *PLoS ONE,* **8**, e56909,
746 https://doi.org/10.1371/journal.pone.0056909, 2013.
747 Chen, X., Škerlak, B., Rotach, M. W., Añel, J. A., Su, Z. B., Ma, Y. M., and Li, M. S.:
748 Reasons for the extremely high-ranging planetary boundary layer over the
749 western Tibetan Plateau in winter. *J. Atmos. Sci.*, **73**, 2021-2038, doi:

10.1175/JAS-D-15-0148.1, 2016.

Crosman, E. T., and Horel, J. D.: Sea and Lake Breezes: A Review of Numerical Studies. *Bound.-Layer Meteor.*, 137(1), 1 – 29. doi:10.1007/s10546-010-9517-9, 2010.

Crosman, E. T., and Horel, J. D.: Idealized Large-Eddy Simulations of Sea and Lake Breezes: Sensitivity to Lake Diameter, Heat Flux and Stability. *Bound.-Layer Meteor.*, **144**, 309-328, https://doi.org/10.1007/s10546-012-9721-x, 2012.

Friehe, C. A., Shaw, W. J., Rogers, D. P., Davidson, K. L., Large, W. G., Stage, S. A., Crescenti, G. H., Khalsa, S. J. S., Greenhut, G. K., and Li, F.: Air-sea fluxes and surface layer turbulence around a sea surface temperature front [J]. J. Geophys. Res., 96(C5): 8593 – 8609. doi:10.1029/90JC02062, 1991.

Foken, T., Matthias, M., Liebethal, C., Wimmer, F., Beyrich, F., Leps, J. P., Raasch, S., DeBruin, H. A. R., Meijninger, W. M. L., Bange, J.: Energy balance closure for the LITFASS-2003 experiment. Theor Appl Climatol., 101(1-2), 149-160. doi:10.1007/s00704-009-0216-8, 2010.

Gray, M. E. B., Petch, J., Derbyshire, S. H., et al. 2001. Version 2.3 of the Met.Office large eddy model: part Ⅱ. Scientific documentation [R]. Met Office (APR) Turbulence and Diffusion Note No.276.

Hadfield, M. G., Cotton, W. R., and Pielke, R. A.: Large-eddy simulations of thermally forced circulations in the convective boundary layer. Part I: A small-scale circulation with zero wind. Boundary-Layer Meteorology, 57(1-2), 79-114. doi:10.1007/bf00119714, 1991.

772 Hadfield, M. G., Cotton, W. R., and Pielke, R. A.: Large-eddy simulations of
773 thermally forced circulations in the convective boundary layer. Part II: The
774 effect of changes in wavelength and wind speed. Boundary-Layer Meteorology,
775 58(4), 307-327. doi:10.1007/bf00120235, 1992.
776 Honnert, R., Masson, V., & Couvreux, F.: A diagnostic for evaluating the
777 representation of turbulence in atmospheric models at the kilometric scale. J.
778 Atmos. Sci., 68 , 3112-3131. doi: 10.1175/JAS-D-11-061.1, 2011.
779 Honnert, R., Efstathiou, G. A., Beare, R. J., et al. The Atmospheric Boundary Layer
780 and the "Gray Zone" of Turbulence: A Critical Review. Journal of Geophysical
781 Research: Atmospheres, 125. doi: 10.1029/2019JD030317, 2020.
782 Huang, Q., Marsham, J. H., Parker, D. J., Tian, W. S., Tammy, W.: A Comparison of
783 Roll and Nonroll Convection and the Subsequent Deepening Moist Convection:
784 An LEM Case Study Based on SCMS Data. Monthly Weather Review, 137(1),
785 350-365. doi:10.1175/2008MWR2450.1, 2009.
786 Jia, D., Wen, J., Ma, Y., Wang, X. and Lai, X.: The warm season characteristics of the
787 turbulence structure and transfer of turbulent kinetic energy over alpine
788 wetlands at the source of the yellow river. Meteorology & Atmospheric Physics,
789 130(1), 1-14. doi: 10.1007/s00703-017-0534-9, 2017.
790 Kang, S. L., and Lenschow, D. H.: Temporal evolution of low-level winds induced by
791 two-dimensional mesoscale surface heat-flux heterogeneity. Boundary-Layer
792 Meteorology, 151: 501–529. doi: 10.1007/s10546-014-9912-8, 2014.
793 Li, W. L., Lü, S. H., Fu, S. M., Meng, X. H., and Nnamchi, H. C.: Numerical

simulation of fluxes generated by inhomogeneities of the underlying surface over the Jinta Oasis in Northwestern China. *Adv. Atmos. Sci*, **28**, 887-906, doi: 10.1007/s00376-010-0041-0, 2011.

Li, Z. G., Lyu, S. H., Ao, Y. H., Wen, L. J., Zhao, L., Wang, S. Y.: Long-term energy flux and radiation balance observations over Lake Ngoring, Tibetan Plateau. *Atmos. Res.*, **155**, 13-25, https://doi.org/10.1016/j.atmosres.2014.11.019, 2015.

Li, Z. G., Lyu, S. H., Wen, L. J., Zhao, L., Ao, Y. H., Wang, S. Y.: Effect of a cold, dry air incursion on atmospheric boundary layer processes over a high-altitude lake in the Tibetan Plateau. *Atmos. Res.*, **185**, 32-43, doi: 10.1016/j.atmosres.2016.10.024, 2017.

Liu, G., Sun, J. N., and Yin. L.: Turbulence characteristics of the shear-free convective boundary layer driven by heterogeneous surface heating. Boundary-Layer Meteorology, 140(1), 57-71. doi: 10.1007/s10546-011-9591-7, 2011.

Liu, R., Liu, S.M., Yang, X.F., Lu, H., Pan, X.D., Xu, Z.W., Ma, Y.F., Xu, T.R.: Wind dynamics over a highly heterogeneous oasis area: an experimental and numerical study. J. Geophys. Res. 123, 8418 – 8440. doi: 10.1029/2018JD028397, 2018.

Liu, R., Sogachev, A., Yang, X., Liu, S., Xu, T., Zhang, J.: Investigating microclimate effects in an oasis-desert interaction zone. Agricultural and Forest Meteorology, 290, 107992. doi: 10.1016/j.agrformet.2020.107992, 2020.

Mahrt, L.: Surface Heterogeneity and Vertical Structure of the Boundary Layer. , 96(1-2), 33–62. doi:10.1023/a:1002482332477, 2000.

816 Maronga, B., and Raasch, S.: Large-eddy simulations of surface heterogeneity effects
817 on the convective boundary layer during the litfass-2003 experiment.
818 Boundary-Layer Meteorology, 146(1), 17-44. doi: 10.1007/s10546-012-9748-z,
819 2013.
820 Marsham, J. H., Parker, D. J., Grams, C. M., Johnson, B. T., Grey, W. M. F., and Ross,
821 A. N.: Observations of mesoscale and boundary-layer scale circulations
822 affecting dust transport and uplift over the Sahara. *Atmos. Chem. Phys*, **8**,
823 6979-6993, https://doi.org/10.5194/acp-8-6979-2008, 2008.
824 Matthias, S., Maronga, B., Florian, H., and Siegfried, R.: On the Effect of Surface
825 Heat-Flux Heterogeneities on the Mixed-Layer-Top Entrainment.
826 Boundary-Layer Meteorology, 151(3), 531-556.
827 doi:10.1007/s10546-014-9913-7, 2014.
828 Moeng, C.-H.: A Large-Eddy-Simulation Model for the Study of Planetary
829 Boundary-Layer Turbulence. *J. Atmos. Sci.*, **41**, 2052-2062,
830 https://doi.org/10.1175/1520-0469(1984)041<2052:ALESMF>2.0.CO;2, 1984.
831 Mudassar, I., Wen, J., Wang, S. P., Tian, H., and Adnan, M.: Variations of precipitation
832 characteristics during the period 1960-2014 in the source region of the Yellow
833 River, China. Journal of Arid Land, 10(3): 388-401.
834 https://doi.org/10.1007/s40333-018-0008-z, 2018.
835 Patil, M. N., Waghmare, R. T., Dharmaraj, T., Chinthalu, G. R., Devendraa, S., and
836 Meena, G. S.: The influence of wind speed on surface layer stability and
837 turbulent fluxes over southern Indian peninsula station. Journal of Earth System

838 Science, 125(7), 1399–1411. doi:10.1007/s12040-016-0735-5, 2016.
839 Patton, E. G., Sullivan, P. P., and Moeng, C. H.: The influence of idealized
840 heterogeneity on wet and dry planetary boundary layers coupled to the land
841 surface. Journal of the Atmospheric Sciences, 62(7), 2078-2097. doi:
842 10.1175/JAS3465.1, 2005.
843 Shao, Y. P., Liu, S. F., Schween, J. H., and Crewell, S.: Large-Eddy
844 Atmosphere-Land-Surface Modelling over Heterogeneous Surfaces: Model
845 Development and Comparison with Measurements. Boundary-Layer
846 Meteorology, 148(2), 333-356. doi: 10.1007/s10546-013-9823-0, 2013.
847 Shen, S. H., and Leclerc, M. Y.: How large must surface inhomogeneities be before
848 they influence the convective boundary layer structure? A case study. Q. .I. R.
849 Meteorol. soc., 121(526), 1209-1228. doi:10.1002/qj.49712152603, 1995.
850 Shen, L. D., Sun, J. N., Yuan, R. M., and Liu, P.: Characteristics of secondary
851 circulations in the convective boundary layer over two-dimensional
852 heterogeneous surfaces. *J. Meteor. Res.*, **30**, 944-960,
853 https://doi.org/10.1007/s13351-016-6016-z, 2016.
854 Sommeria, G., and LeMone, M. A.: Direct testing of a three-dimensional model of the
855 planetary boundary layer against experimental data. *J. Atmos. Sci.,* **35**, 25-39,
856 https://doi.org/10.1175/1520-0469(1978)035<0025:DTOATD>2.0.CO;2, 1978.
857 Sullivan, P. P., Moeng, C., Stevens, B., Lenschow, D. H., and Mayor, S. D.: Structure
858 of the Entrainment Zone Capping the Convective Atmospheric Boundary Layer,
859 Journal of the Atmospheric Sciences, 55(19), 3042-3064.

https://doi.org/10.1175/1520-0469(1998)055<3042:SOTEZC>2.0.CO;2, 1998.

Tyagi, B., and Satyanarayana, A. N. V.: The Budget of Turbulent Kinetic Energy during Premonsoon Season over Kharagpur as Revealed by STORM Experimental Data. *ISRN Meteorology*, **2013**, 1-11, doi: 10.1155/2013/972942, 2013.

Wang, B. B., Ma, Y. M., Chen, X. L., Ma, W. Q., Su, Z. B., and Menenti, M.: Observation and simulation of lake–air heat and water transfer processes in a high-altitude shallow lake on the Tibetan Plateau [J]. J. Geophys. Res., 120(24): 12327-12344. doi:10.1002/2015JD023863, 2015.

Wang, C., Tian, W. S., Parker, D. J., Marsham, J. H. and Guo, Z.: Properties of a simulated convective boundary layer over inhomogeneous vegetation. *Quart. J. Roy. Meteor. Soc*., **137**, 99-117, https://doi.org/10.1002/qj.724, 2011.

Wang, Y., Xu, X., Liu, H., et al., Wang, Y. J., Xu, X. D., Liu, H. Z., Li, Y. Q., Li, Y. H., Hu, Z. Y., Gao, X. Q., Ma, Y. M., Sun, J. H., Lenschow, D. H., Zhong, S. Y., Zhou, M. Y., Bian, X. D., and Zhao, P.: Analysis of land surface parameters and turbulence characteristics over the Tibetan Plateau and surrounding region. *J. Geophys. Res.: Atmospheres*, **121**, 9540-9560, doi:10.1002/2016JD025401, 2016.

Wen, L. J., Lyu, S. H., Li, Z. G., Zhao, L., and Nagabhatla, N.: Impacts of the Two Biggest Lakes on Local Temperature and Precipitation in the Yellow River Source Region of the Tibetan Plateau. *Adv. Meteor.*, **2015**, 10, doi:10.1155/2015/248031, 2015.

Wen, L. J., Lyu, S. H., Kirillin, G., Li, Z. G., and Zhao, L.: Air-lake boundary layer

and performance of a simple lake parameterization scheme over the Tibetan highlands, Tellus A: Dynamic Meteorology and Oceanography, 68:1, 31091. doi: 10.3402/tellusa.v68.31091, 2016.

Xu, Z. W., Ma, Y. F., Liu, S. M., Shi, W. J., Wang, J. M.: Assessment of the Energy balance closure under advective conditions and its impact using remote sensing data. Journal of Applied Meteorology and Climatology, 56(1). doi:10.1175/JAMC-D-16-0096.1, 2016.

Zhang, W. C., Guo, J. P., Miao, Y. C., Liu, H., Song, Y., Fang, Z., He, J., Lou, M. Y., Yan, Y., Li, Y., and Zhai, P. M.: On the summertime planetary boundary layer with different thermodynamic stability in China: A radiosonde perspective [J]. J. Climate, 31(4): 1451-1465. doi:10.1175/JCLI-D-17-0231.1, 2018.

Zhao, Y., Xu, X. D., Ruan, Z., Chen, B., and Wang, F.: Precursory strong-signal characteristics of the convective clouds of the Central Tibetan Plateau detected by radar echoes with respect to the evolutionary processes of an eastward-moving heavy rainstorm belt in the Yangtze River Basin. *Meteor. Atmos. Phys.,* 1-16, https://doi.org/10.1007/s00703-018-0597-2, 2018.

Zheng, D. H., Velde, R. V. D., Su, Z. B., Wang, X., Wen, J., Booij, M. J., Hoekstra, A. Y., and Chen, Y. Y.: Augmentations to the Noah Model Physics for Application to the Yellow River Source Area. Part II: Turbulent Heat Fluxes and Soil Heat Transport. *J. Hydromete.*, **16**, 2677-2694, https://doi.org/10.1175/JHM-D-14-0199.1, 2015.

Zhou, Y., Li. D., Liu, H. and Li, X.: Diurnal variations of the flux imbalance over

homogeneous and heterogeneous landscapes. Boundary-Layer Meteorology, 168:417 – 442. https://doi.org/10.1007/s10546-018-0358-2, 2018.